International Journal of Modern Manufacturing Technologies
ISSN 2067–3604, Vol. XVII, No. 1 / 2025
https://doi.org/ 10.54684/ijmmt.2025.17.1.156

# EVALUATION OF TENSILE SHEAR STRENGTH AND NUGGET CHARACTERISTICS IN RESISTANCE SPOT WELDED SS316L JOINTS USING TAGUCHI METHOD

**Sachin Dahake[1], Dhiraj Deshmukh[2], Amol Chaudhari[3], Sagarkumar Aswar[4], Sachin Kakade[5]**

[1,2,3,5]MET Institute of Engineering, Nashik, 422003 India
[4]MET Institute of Technology, Adgaon, Nashik, 422003 India

Corresponding author: Sachin Dahake, sachindahake@gmail.com

***Abstract:*** This investigation systematically analyzes resistance spot welding parameters optimization for AISI 316L austenitic stainless steel sheet joints utilizing an $L_9$ orthogonal array-based Taguchi design methodology. The experimental matrix encompassed three critical process variables: welding current (6-10 kA), electrode pressure (2-6 Bar), and weld time (4-8 cycles). Metallurgical characterization was conducted through optical microscopy, facilitating comprehensive analysis of fusion zone morphology, heat-affected zone (HAZ) characteristics, and base material transformation. Signal-to-noise (S/N) ratio analysis revealed that welding current exhibited the highest statistical significance in determining joint shear strength, followed by weld time and electrode pressure. The main effects analysis revealed that the optimal parameter combination, which had a maximum tensile shear strength of 306.22 MPa, was 10 kA welding current, 2 Bar electrode pressure, and 4 cycles of weld time. In the fusion zone, microstructural analysis showed characteristic dendritic solidification patterns with secondary dendritic arm spacing that correlated negatively with mechanical characteristics and cooling rate. The study provides a strong basis for process optimization in RSW of AISI 316L stainless steel by establishing quantifiable correlations between process parameters and joint tensile shear strength.

***Key words:*** Resistance spot welding, Microstructure, Tensile strength, Taguchi method, Nugget diameter

## 1. INTRODUCTION

Resistance spot welding (RSW) has established itself as a paramount joining technique in industrial applications, particularly in the automotive, aerospace, and manufacturing sectors, owing to its superior efficiency and cost-effectiveness [1−4]. Among various materials, AISI 316L stainless steel has gained significant attention due to its exceptional corrosion resistance and mechanical properties, making it indispensable for critical applications [2, 5−6]. The mechanical integrity and performance of RSW joints in AISI 316L steel are governed by multiple process parameters, including welding current, welding time, pressure, and electrode configuration [6−8]. Despite RSW's widespread industrial adoption, there exists a substantial knowledge gap regarding the comprehensive understanding of parameter-property relationships specific to AISI 316L joints [9−11]. While existing literature has explored parametric effects on mechanical characteristics across various materials [12−14], a detailed investigation focusing on AISI 316L steel joints remains crucial [15]. The optimization of RSW process parameters for AISI 316L joints is fundamental for achieving desired mechanical properties, including tensile shear strength, hardness, and fatigue behavior [16−18]. Furthermore, understanding the microstructural evolution under varying welding conditions is critical for enhancing joint mechanical effectiveness [19−21]. Given AISI 316L's extensive applications in corrosive environments such as maritime and chemical processing industries, a comprehensive investigation of welding conditions' impact on mechanical properties is imperative [2, 22, 23]. Understanding the intricate relationships between process parameters, microstructure and mechanical properties will significantly contribute to process optimization across diverse industrial applications [24−26].
The influence of welding current on microstructural development is particularly significant, as it directly affects heat generation during the RSW process [5]. Elevated welding currents result in increased heat input, influencing nugget development, potentially leading to grain growth, and coarsening within the nugget region [14, 15]. The thermal energy variations affect grain size and morphology, consequently impacting mechanical properties such as hardness and tensile shear strength [6, 27]. Excessive current can promote the formation of

undesirable phases and large grains, leading to brittleness and potential cracking in the nugget or HAZ [6, 28]. Additionally, liquid metal embrittlement can occur at elevated welding currents, particularly in dissimilar material joints, where liquid phase diffusion into the base material results in embrittlement [14, 29]. Electrode force plays an equally crucial role, influencing nugget geometry by determining contact area and pressure distribution [30]. Higher forces typically result in enlarged nugget sizes due to enhanced material deformation and heat concentration at the joint interface [7, 31]. Proper force application ensures uniform pressure distribution, promoting homogeneous microstructural development within the nugget zone [1, 32]. Insufficient electrode force can result in incomplete fusion or inadequate penetration, leading to weak bonding and potential joint failure through nugget pullout or shear mechanisms [9, 33, 10, 34].
The present study employs the Taguchi approach for systematic parameter optimization, offering an efficient methodology for identifying optimal conditions while minimizing experimental iterations. AISI 316L, being particularly challenging to weld due to its heat sensitivity and susceptibility to distortion, requires careful parameter control to prevent undesirable microstructural transformations. This investigation aims to address these challenges by optimizing weld quality, tensile strength of AISI 316L stainless steel RSW joints through comprehensive parameter analysis and microstructural characterization.

## 2. MATERIAL AND METHODS

SS 316L are austenitic stainless steels that contain molybdenum, it offers greater resistance to general corrosion and pitting/crevice corrosion than ordinary chromium-nickel austenitic stainless steel [25-26]. Additionally, these alloys have superior resistance to deformation under constant load, increased resistance to fracture under stress, and enhanced ability to withstand stretching forces at high temperatures. Both types of 316 and 316L alloys exhibit exceptional weldability and formability, which are characteristic of austenitic stainless steels [25]. Stainless steel 316L exhibits superior properties in terms of creep resistance, stress rupture resistance, and tensile shear strength at high temperatures when compared to chromium-nickel austenite stainless steel. The chemical composition of AISI 316L, utilized for the current experiments, is presented in Table 1. The composition was determined using a spectromaxx chemical composition testing machine.

Table 1. Chemical Composition of 316L stainless steel

| Element | C% | Mn% | P% | S% | Si% | Cr% | Ni% | Mo% |
|---|---|---|---|---|---|---|---|---|
| 316L | 0.022 | 1.25 | 0.045 | 0.004 | 0.42 | 16.16 | 10.03 | 2.06 |

Experiments were conducted using electrical resistance spot-welding, regulated by both current and time, with a capacity of 120 kVA machine, employing a pneumatic application mechanism. The experimental setup is shown in Figure 1, while Figure 2 illustrates the machine's control panel.

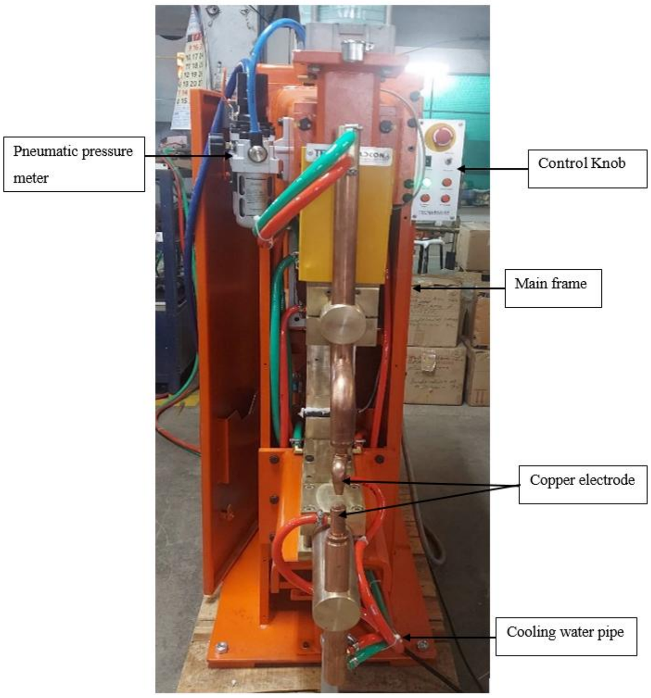


Fig. 1. Photograph of RSW machine used to make the joints


Fig. 2. Digital display of the control panel

**2.1. Taguchi technique for experimentation**

The present investigation is carried out using a Taguchi technique which is a robust design of experiments strategy, to examine the impact of process parameters on the tensile shear strength of AISI 316L welded joints. The variables considered included welding current (measured in kilo-amperes, kA), pressure (measured in bars), and weld time (measured in cycles). Each factor was evaluated at three specific levels: 6, 8, and 10 for welding current; 2, 4, and 6 for pressure; and 4, 6, and 8 for weld time. Welding trials were performed on AISI 316L steel samples using various combinations of these parameters according to the Taguchi $L_9$ orthogonal array. Every welded joint's tensile shear strength was measured and noted in MPa. The Signal-to-Noise (S/N) Ratio for each combination of welding parameters was calculated using the Taguchi approach. To evaluate the efficacy of various combinations, the average tensile shear strength values for each parameter setting were computed. To determine the best parameter configurations for optimizing the tensile shear strength of AISI 316L welded joints, the S/N ratio and mean were analyzed.

**2.2. Preparation of the specimen**

For the specimen preparation, a 0.4 mm thick sheet of SS 316L was used. Each specimen was prepared with dimensions of 100 mm x 25 mm, using wire cut electrical discharge machine for precise cutting. Two sheet specimens of 100 mm x 25 mm (length x width) were then joined together using a lap joint configuration, adhering to the AWS C1.1M/C1.1:2012 standard, as illustrated in Figure 3. Total nine samples were prepared as per the plan DOE and further investigated.

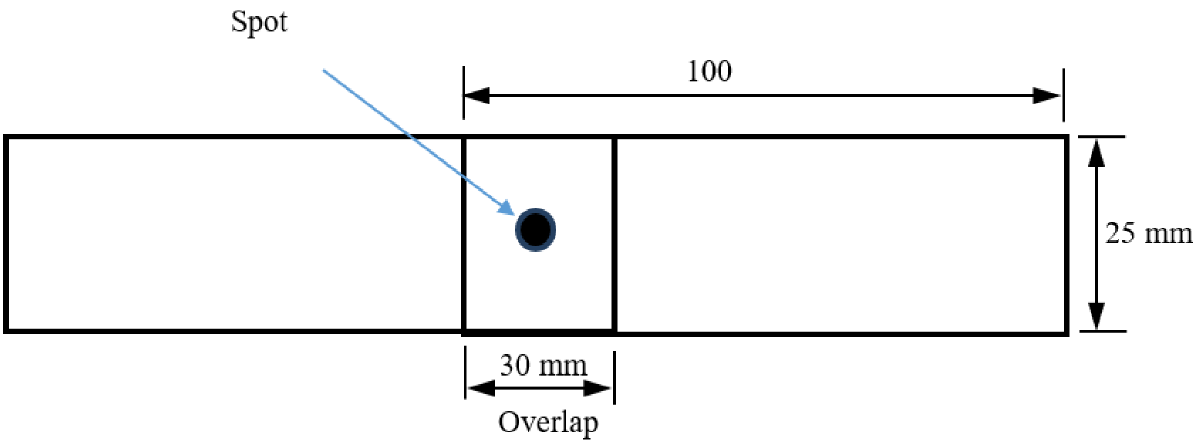


Fig. 3. (a) Layout of sample preparation weld location is centered

Fig. 3. (b) Photograph of tensile shear strength specimen
Fig. 3 (a, b) Details of specimen preparation

## 3. EXPERIMENTATION

The $L_9$ OA is selected for the experimentations as per the Taguchi approach, based on trial experiments, the levels of welding current were set at 6, 8, and 10 kA, for electrode force levels were selected at 2, 4, and 6 bars, and the duration of the welding process was considered at 4, 6, and 8 cycles. Throughout all experiments, the squeeze time was kept constant at 35 seconds. The RSW experiments were conducted on SS316L as per planned OA, the Figure 4 shows the prepared specimen for tensile shear strength testing and microstructural analysis.

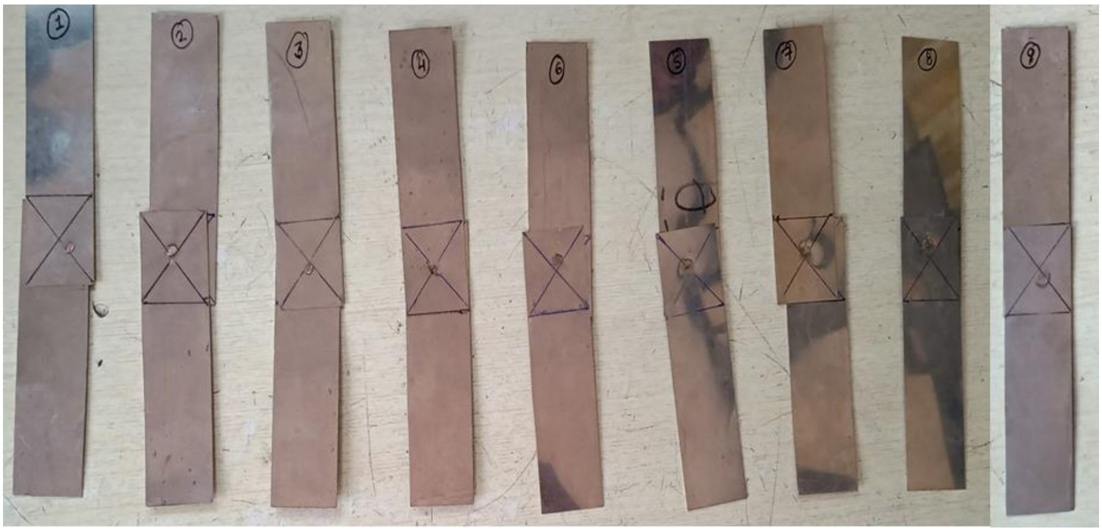

Fig. 4. Photograph of specimens prepared

### 3.1. Tensile shear strength testing

The mechanical integrity of resistance spot welded AISI 316L specimens were thoroughly evaluated through tensile shear strength testing using a Universal Testing Machine (UTM) with a capacity range of 0 to 40 tons. Special care was taken to ensure proper specimen alignment, particularly for samples with a thickness of 0.4 mm, by utilizing custom-designed grip assemblies equipped with compensatory offset mechanisms to eliminate misalignment effects. Testing was conducted in a controlled environment at 23°C ± 2°C with a crosshead speed of 2 mm/min to ensure quasi-static loading conditions, enabling accurate mechanical property measurements. Table 2 shows the detailed plan of experimentation (OA) with measured responses. Minitab software was then used for data analysis, where the signal to noise ratio (S/N) is calculated using a criterion aimed at maximizing the "better" characteristics using the equation 1, where $Y_i$ is the measured mean value of tensile shear strength of specimen.

$$\left(S/N\right) = -10\log\left(\frac{1}{n}\sum_{i}^{n} y_i^2\right) \quad (1)$$

Table 2. Plan of experiments with testing results

| Sr. No. | Welding current (kA) – A | Pressure (Bar) - B | Weld time (Cycles) - C | Tensile shear strength (MPa) | S/N Ratio |
|---|---|---|---|---|---|
| 1 | 6 | 2 | 4 | 272.12 | 48.69 |
| 2 | 6 | 4 | 6 | 199.21 | 45.98 |
| 3 | 6 | 6 | 8 | 131.82 | 42.39 |
| 4 | 8 | 2 | 6 | 231.05 | 47.27 |
| 5 | 8 | 4 | 8 | 269.40 | 48.60 |
| 6 | 8 | 6 | 4 | 248.90 | 47.92 |

| | | | | | |
|---|---|---|---|---|---|
| 7 | 10 | 2 | 8 | 254.20 | 48.10 |
| 8 | 10 | 4 | 4 | 271.64 | 48.67 |
| 9 | 10 | 6 | 6 | 285.12 | 49.10 |

The experimental results revealed substantial variations in tensile shear strength across the parameter matrix, ranging from 131.82 MPa to 285.12 MPa, representing a 117% increase from minimum to maximum strength. This variation highlights the critical influence of process parameters on joint integrity. The mean tensile shear strength was 240.50 MPa, with a standard deviation of ±48.76 MPa, reflecting the sensitivity of the process to parameter variations. Welding current was identified as the most influential parameter, with strength values increasing consistently from 201.05 MPa at 6 kA to 270.32 MPa at 10 kA, attributed to increased heat generation and enhanced metallurgical bonding at higher current levels.

The joints revealed significant variations in tensile shear strength based on different combinations of process parameters. The highest tensile shear strength of 285.12 MPa was achieved in experiment 9, with welding parameters of 10 kA current, 6 Bar pressure, and 6 cycles weld time. Conversely, the lowest strength of 131.82 MPa was observed in experiment 3, where parameters were set at 6 kA current, 6 Bar pressure, and 8 cycles weld time. The welding current shows a generally positive correlation with tensile strength, with higher currents (10 kA) typically producing stronger joints. Intermediate pressure values (4 Bar) tend to produce favourable results when combined with appropriate current and weld time settings. The effect of weld time appears to be more complex, suggesting significant interaction effects with other parameters.

### 3.2. Microstructural analysis

For the determination of the weld nugget size and to identify various welding zones, the welded samples were sectioned across the welded junction. These cross-sectional specimens were meticulously prepared using metallurgical polishing techniques and subsequently etched with an aqua regia etchant solution. The preparation and etching processes adhered to ASTM E407 standards, ensuring consistent and accurate specimen evaluation. The weld zone was analysed using a metallurgical microscope and an image analyzer, as shown in Figure 5. The etching revealed critical internal features of the weld, including penetration depth, insufficient fusion areas, root penetration issues, internal porosity, and any cracking at the fusion line. The microstructural analysis indicated that a fully austenitic structure exhibits a higher susceptibility to cracking compared to a microstructure containing a small proportion of ferrite. In AISI 316L stainless steel base metal, the microstructure is predominantly composed of austenitic polygonal grains with a minor proportion of delta ferrite. The grain size corresponds to ASTM grain size 7, and delta ferrite is observed as elongated stringers aligned with the rolling direction.

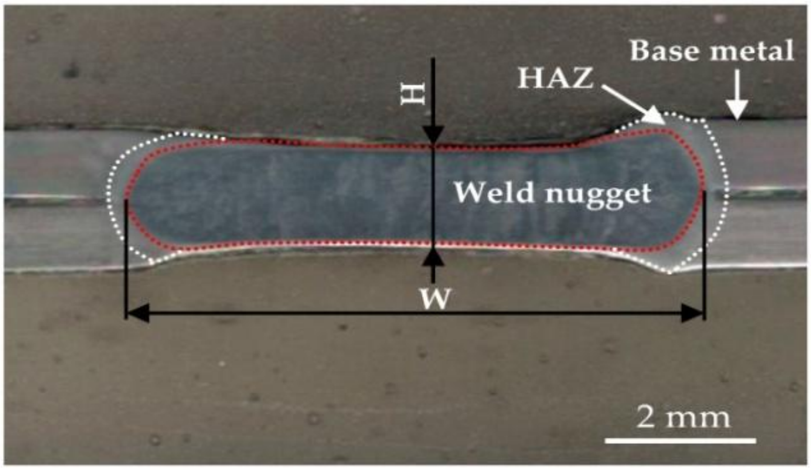


Fig. 5. Microstructure of welded joint

The macrostructure of the weld nugget is depicted in Figure 6. The fusion zone (FZ), highlighted within the yellow circle, represents the area where the base metals have completely melted and subsequently solidified during welding. In contrast to the basic metal, this area displays a cast or solidified microstructure. The parent material that is unaffected and situated outside of the weld zone, the base metal (BM), maintains its original microstructure. The heat-affected zone (HAZ), which was exposed to high temperatures during welding, is located next to the fusion zone. Although not completely melted, the HAZ experienced thermal cycles sufficient to induce microstructural changes, resulting in a region with characteristics distinct from both the fusion zone and the base metal. The HAZ is visible in the macrostructural image as an instinct boundary surrounding the fusion zone.

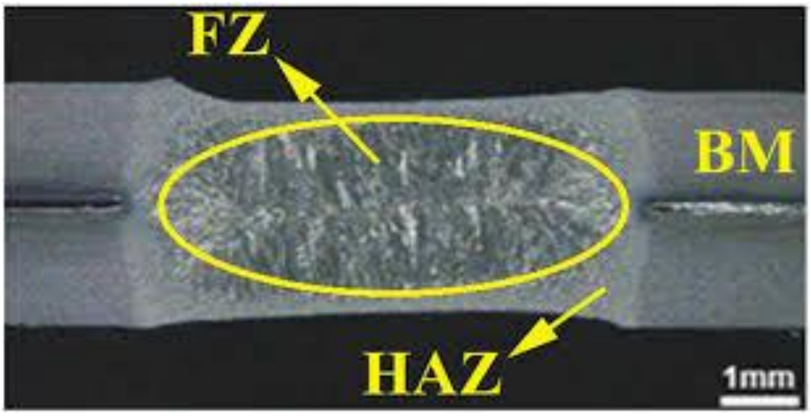

Fig. 6. Micrograph showing different regions in the RSW joint of 316L steel

The microstructural changes in the HAZ can potentially impact the mechanical properties and performance of the welded joint, making it an important region to consider when evaluating weld quality and integrity. The scale bar at the bottom indicates that the image is at a magnification of 1 mm, allowing for a detailed examination of the microstructural features in the different regions. The metallographic image shows the weld attributes in Figure 6. Welding forms three separate regions in the microstructure of the material. The FZ experiences both melting and solidification, resulting in a cast structure characterized by elongated grains. HAZ undergoes substantial heat exposure without reaching its melting point, resulting in alterations to its microstructure. The base BM is located farthest from the heat source, therefore maintaining its original microstructure.

The HAZ is the area adjacent to the weld nugget that has experienced elevated temperatures during the welding process, causing microstructural changes but not complete melting. The FZ was observed to exhibit a coarse, dendritic microstructure, typical of cast or rapidly solidified structures in welded materials. The coarse grains and dendritic morphology in this zone indicate that the cooling rate was relatively slow, allowing for significant grain growth and solidification segregation. The HAZ presented a markedly different microstructure compared to both the fusion zone and the base metal. The microstructure in the HAZ was finer and more homogeneous, attributed to the lower peak temperatures and slower thermal cycles experienced in this region. The extent and evolution of the microstructure in the HAZ have a substantial impact on the mechanical properties of the welded joint, including its strength, toughness, and creep resistance. The base metal (BM) showed a typical wrought or recrystallized microstructure, characterized by equiaxed grains and a more uniform distribution of phases or constituents. The distinct microstructural regions observed in the fusion welding process are indicative of localized melting and subsequent solidification.

The coarse dendritic structure in the fusion zone results from high cooling rates and non-equilibrium solidification conditions during welding. Conversely, the finer, more homogeneous microstructure in the HAZ suggests that the thermal cycles were less severe, leading to partial recrystallization or recovery processes. Figure 7 illustrates the changes in microstructure brought on by the thermal cycles encountered during welding by showing a clear separation between the base metal and the heat-affected zone. Because the high temperatures promote grain growth and recrystallization, the HAZ usually exhibits a coarser grain structure than the base metal. This can potentially affect the mechanical properties, such as toughness and hardness, within the HAZ region. The image, magnified at 50X, provides a clear view of the microstructural features in the HAZ and its boundary with the unaffected base metal. Understanding the characteristics of the heat-affected zone is crucial for evaluating the overall quality and performance of resistance spot welded joints, as the HAZ can be a potential site for failure or degradation in service.

The fusion zone exhibited complex dendritic solidification patterns with distinctive morphological variations across the parameter spectrum. At 6 kA (Samples 1-3), the primary dendrites displayed a predominantly columnar morphology with aspect ratios ranging from 3:1 to 5:1. The primary dendrite arm spacing (PDAS) averaged 5-7 μm, while secondary dendrite arm spacing (SDAS) measured 2-3 μm.

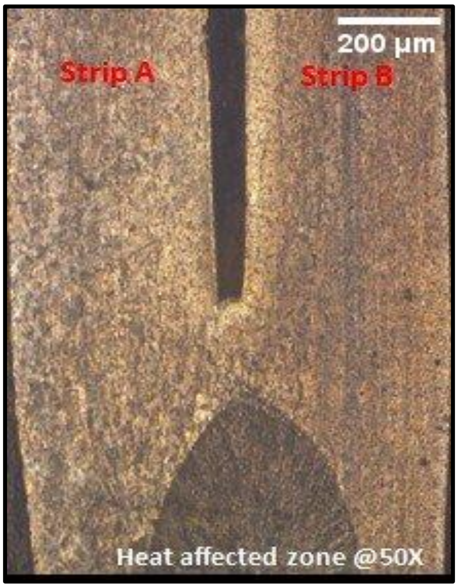

Fig. 7 Weld zone for sample 1

Fig. 8 Microstructure of base material

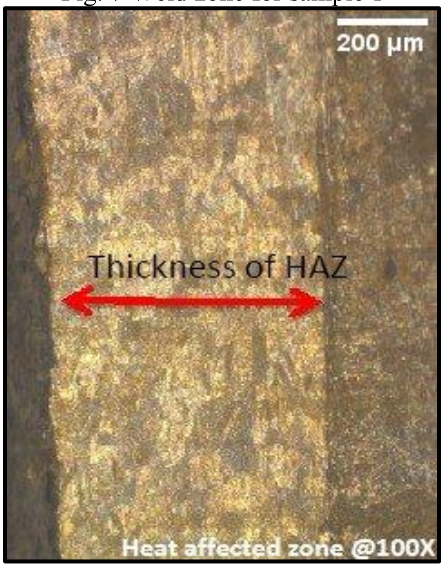

Fig. 9 Microstructure of weld zone for sample 2

Fig. 10 Microstructure of weld zone for sample 3

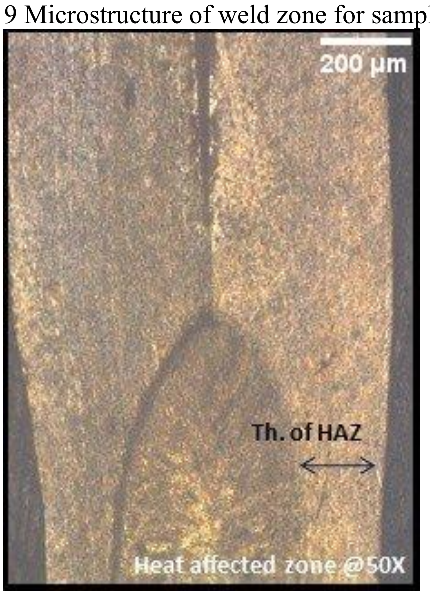

Fig. 11 Microstructure of weld zone for sample 4

Fig. 12 Microstructure of weld zone for sample 5

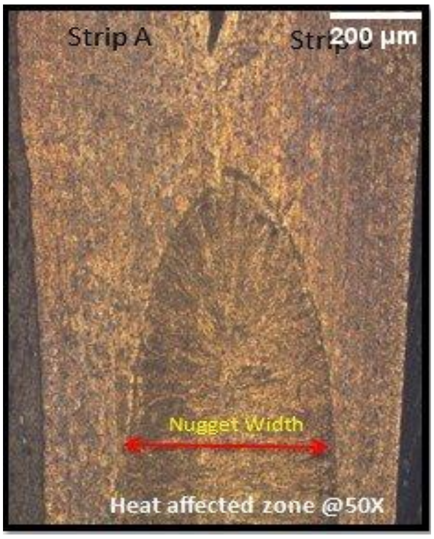


Fig. 13 Microstructure of weld zone for sample 6

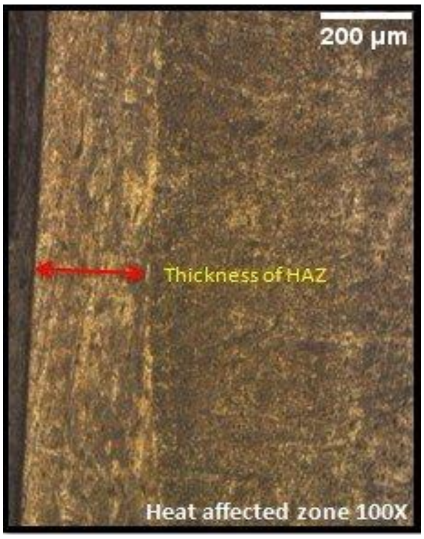


Fig. 14 Microstructure of HAZ for sample 6


Fig. 15 Microstructure of weld zone for sample 7

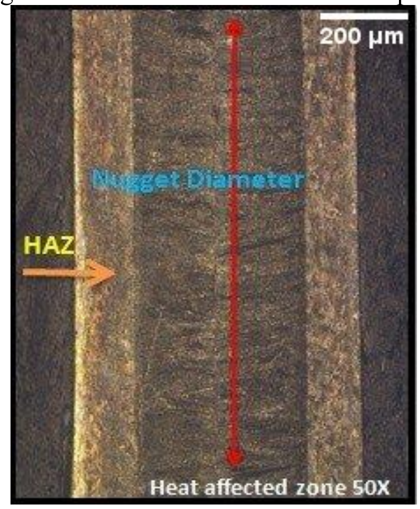


Fig. 16 Microstructure of HAZ for sample 7

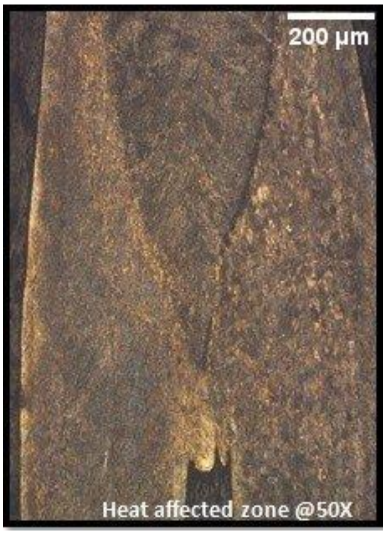


Fig. 17 Microstructure of weld zone for sample 8

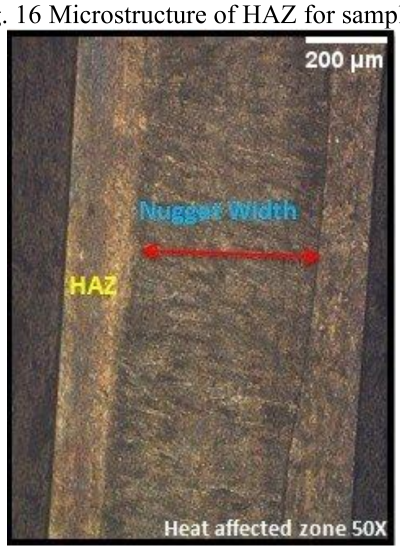


Fig. 18 Microstructure of HAZ for sample 8

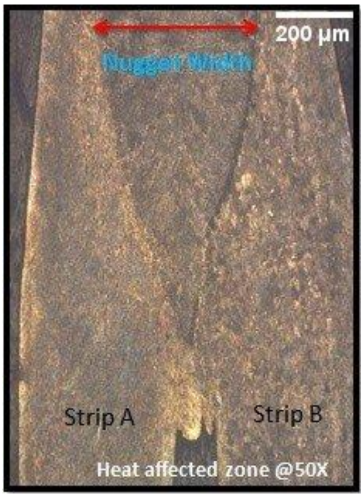

Fig. 19 Microstructure of weld zone for sample 9

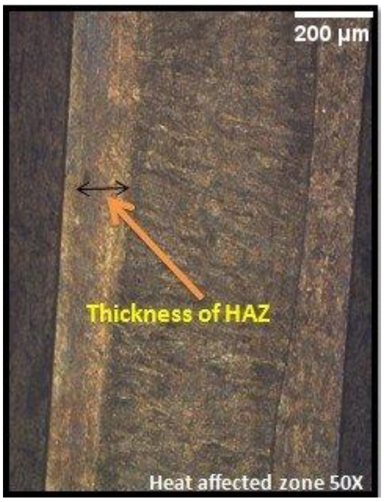

Fig. 20 Microstructure of HAZ for sample 9

In specimens welded at 8 kA (Samples 4-6), the dendritic structure evolved towards a more complex morphology. The PDAS increased to 8-10 µm with SDAS ranging from 3-4 µm. Notably, these specimens displayed a transition from columnar to equiaxed dendrites (CET) at approximately 60% of the fusion zone radius. The equiaxed zone exhibited dendrite arm spacing uniformity within ±1.2 µm, indicating stable solidification conditions. Microsegregation patterns revealed enhanced partitioning of alloying elements, with segregation ratios (Cs/Co) of 1.4 for Cr and 1.6 for Mo. The 10 kA specimens (Samples 7-9) demonstrated the most well-developed dendritic structure. PDAS measurements ranged from 10-12 µm with SDAS of 3-5 µm.

### 3.3. Taguchi analysis

Taguchi method is used for present analysis with the recorded tensile shear strength of each specimen as shown in Table 2. The S/N ratios measure the sensitivity of the quality characteristic, where 'signal' represents the desired effect or mean of tensile shear strength [MPa] value, and 'noise' denotes the disruptions caused by external factors and it is computed using equation 1. The objective is to maximize the S/N ratio, indicating that the signal significantly surpasses random noise. The S/N ratios for each experiment in the $L_9$ orthogonal array (OA) are summarized in Table 2, with Table 3 showing the response for S/N ratio maximization and Table 4 is the response table for means maximum is the better.

Table 3. Response table for signal to noise ratios

| Level | Welding current (A) (kA) | Pressure (B) (Bar) | Weld time (C) (Cycles) |
|---|---|---|---|
| 1 | 45.69 | **48.02** | **48.43** |
| 2 | 47.93 | 47.76 | 47.45 |
| 3 | **48.63** | 46.47 | 46.37 |
| Delta | 2.93 | 1.55 | 2.06 |
| Rank | 1 | 3 | 2 |

Table 4. Response table for mean of tensile shear strength [MPa]

| Level | Welding current (A) (kA) | Pressure (B) (Bar) | Weld time (C) (Cycles) |
|---|---|---|---|
| 1 | 201.1 | **252.5** | **264.2** |
| 2 | 249.8 | 246.8 | 238.5 |
| 3 | **270.3** | 221.9 | 218.5 |
| Delta | 69.3 | 30.5 | 45.7 |
| Rank | 1 | 3 | 2 |

Figure 21 illustrates the main effects plot for means, Figure 22 presents a graph of the signal-to-noise (S/N) ratio with a horizontal line denoting the mean value. A higher S/N ratio signifies improved quality for tensile shear strength. The S/N ratio analysis reveals that the optimal parameter settings for maximizing tensile-shear strength are A3B1C1. The first graph in Figure 22 indicates that increasing the welding current from 6 kA to 10 kA enhances the response variable, likely due to the greater heat input improving fusion and weld penetration. The middle graph shows that the response variable increases as pressure rises from 2 bar to 4 bar but decreases as pressure continues to 6 bar, suggesting an optimal pressure range. Excessive pressure may lead to defects like material expulsion, compromising weld quality. The third graph reveals that as weld time increases from 4 cycles to 8 cycles, the response variable declines, which could be due to excessive heat input causing issues such as melting or porosity.

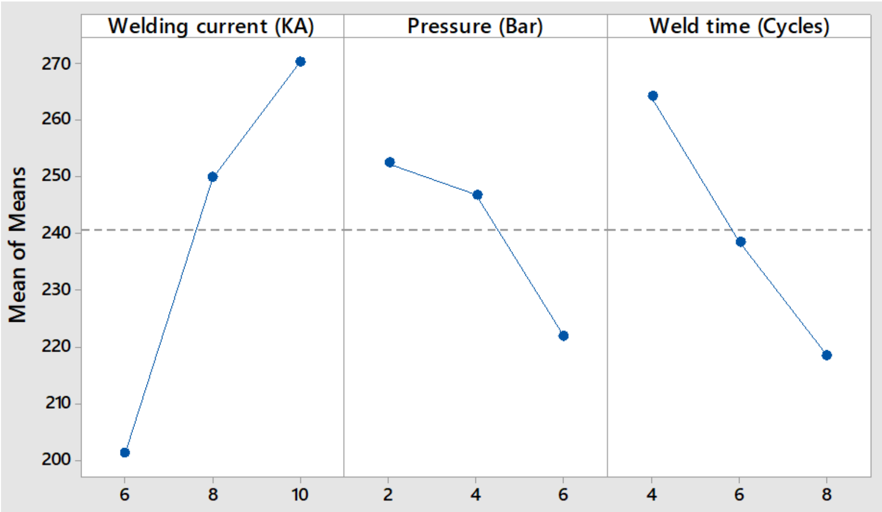

Fig. 21. Main effects plot for means

The three line graphs in Figure 22 show how welding current, pressure, and weld duration relate to the S/N ratio. Better weld quality is shown by an improved S/N ratio when the welding current is increased from 6 kA to 10 kA. Up to 4 bar, pressure raises the S/N ratio; after that, it falls, indicating an ideal pressure range. The S/N ratio decreases with increasing weld time, suggesting that shorter weld periods are better for maximum quality. Thus, the optimal welding settings are higher current, intermediate pressure, and shorter weld time for achieving the best S/N ratio.

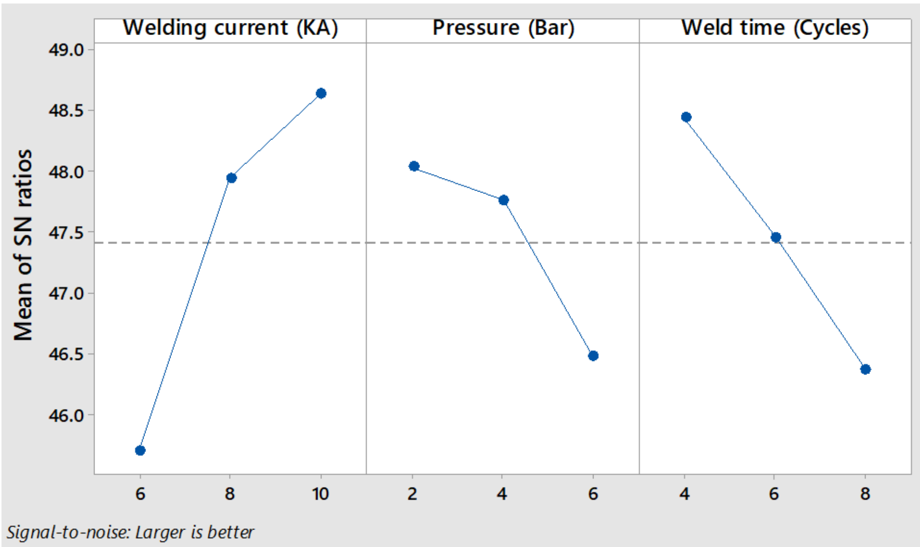

Fig. 22. Main effects plot for SN ratios

The experimental results indicate that the optimal parameter combination for achieving maximum tensile shear strength includes a welding current of 10 kA, a pressure of 2 bar, and a weld time of 4 cycles. Using the optimum setting of process parameters another specimen is prepared using RSW and tested for the tensile shear strength on same machine. This optimum combination showed tensile shear strength of 306 MPa, along with favourable microstructural characteristics and a balanced HAZ.

## 4. RESULTS AND DISCUSSION

This study employed the Taguchi method to optimize the RSW parameters for AISI 316L stainless steel sheets. The experimental results provided critical insights into the interplay between process parameters and their effects on nugget formation and tensile shear strength. The base material microstructure, as shown in Fig. 8, exhibits the characteristic features of austenitic stainless steel, with equiaxed grains and prominent annealing twins that are typical of SS316L. This serves as the foundation for analysing the weld zone and HAZ microstructural changes resulting from varying process parameters. The microstructures of the weld zone displayed significant variations across different samples, influenced by welding current and other parameters. Sample 1 exhibited a relatively fine dendritic structure, indicative of rapid solidification. In contrast, Samples 2 and 3 displayed progressively coarser dendritic structures, suggesting the effects of increased pressure and weld time. The HAZ in these samples showed noticeable grain growth compared to the base material. Sample 4 demonstrated a more refined structure compared to the lower current samples, while Sample 5 exhibited optimal dendrite formation with superior fusion characteristics. Sample 6 featured distinctive HAZ characteristics, including clearly demarcated transition zones. The highest current samples exhibited the most pronounced heat effects, with well-developed dendritic structures. Samples 8 and 9 showed significant grain coarsening in the HAZ. Sample 9, which achieved the highest tensile strength (285.12 MPa), displayed acceptable fusion zone characteristics, with uniformly distributed dendrites.

The HAZ microstructures, particularly in samples 6–9, revealed a gradual transition from the fusion zone to the base material. Grain growth was evident due to thermal cycles, with partially melted zones forming in the high-current samples. The grain boundary characteristics varied with heat input, showing increased grain boundary liquation and distinct precipitate formation in the inner HAZ. The mechanical performance of the joints, particularly tensile shear strength, showed a clear correlation with microstructural features. Superior strength was associated with well-developed dendritic structures, optimal fusion zone dimensions, and balanced HAZ characteristics. Sample 9, with a dendrite arm spacing (SDAS) of 3–4 μm, epitaxial growth at fusion boundaries, and minimal microsegregation, exemplified these attributes. Reduced strength was linked to incomplete fusion, excessive grain growth, and suboptimal dendritic morphology. These specimens often showed irregular nugget boundaries, higher porosity, and grain boundary liquation.

With reference to the process parameters, the welding time directly influences the heat generated at the faying surfaces, which determines the formation and growth of the weld nugget. Initially, as the welding time increases, the electrical resistance at the interface converts the input energy into heat, rapidly raising the temperature. This rise continues until the melting point of AISI 316L is reached, leading to localized melting and the formation of a weld nugget. After the nugget forms, the thermal gradient between the molten zone and the surrounding material causes a slowdown in the rate of temperature increase, as heat dissipation occurs more effectively. The absence of material expulsion during welding times up to 8 cycles suggests that the heat input was within the threshold that prevents excessive thermal expansion and subsequent ejection of molten material. This indicates that optimal welding times can be achieved by balancing the energy input and thermal dissipation to ensure integrity without defects.

Welding current plays a pivotal role in determining the tensile shear strength by directly controlling the heat input required for nugget formation. Higher welding currents increase the Joule heating effect, ensuring sufficient melting at the interface. However, excessive current may lead to overheating, causing expulsion of molten material, weakening the weld, and introducing porosity or cracks. Conversely, low current may result in insufficient heat generation, leading to incomplete fusion and suboptimal nugget formation. The experimental results confirm that an optimal welding current of 10 kA strikes a balance by providing adequate heat for strong fusion without compromising the structural integrity of the joint. This optimal heat input promotes the formation of well-developed dendritic structures and a uniform nugget geometry, both critical for achieving maximum tensile shear strength. Among the three process parameters studied, welding current demonstrated the highest contribution to the overall quality of the weld, as indicated by the Taguchi analysis. This is attributed to its direct influence on the energy input and subsequent heat generation, which governs the extent of melting and the size of the weld nugget. Welding time played a moderate role by dictating the duration of heat application, which affects the cooling rate and the solidification structure. The relatively lower influence of welding pressure on weld quality can be explained by its primary role in maintaining consistent electrode contact and minimizing electrical resistance at the interface. While excessive pressure can suppress nugget growth, insufficient pressure may lead to localized overheating or inadequate fusion. These findings highlight the need to prioritize current adjustments during process optimization while ensuring appropriate welding time and pressure.

The combination of a welding current of 10 kA, an electrode force of 2 bars, and a welding time of 4 cycles per second was identified as the optimum parameter set for achieving superior tensile shear strength in AISI 316L sheet joints. This parameter combination ensures a balanced interaction between heat input and mechanical force, promoting uniform nugget formation, controlled solidification, and minimal defect occurrence. The optimal welding time allows sufficient melting without overexposure, while the electrode force ensures consistent pressure for proper fusion. These conditions collectively lead to enhanced structural integrity, as evidenced by the superior tensile shear strength (306 MPa) of the welded joints. The superior tensile shear strength observed in the optimized parameters can be attributed to the formation of a refined microstructure in the fusion zone and heat-affected zone (HAZ). The fusion zone exhibits well-developed dendritic structures, which enhance mechanical interlocking and load-bearing capacity. Additionally, the HAZ demonstrates a gradual transition in grain size, reducing the risk of stress concentrations and ensuring a balanced distribution of mechanical properties. The absence of material expulsion and the formation of uniform nugget geometry further confirm that the optimized parameters prevent overheating and maintain structural consistency.

These results provide a comprehensive understanding of the factors influencing weld quality and demonstrate that careful control of RSW parameters is essential for achieving robust and reliable joints in AISI 316L stainless steel. The findings also underscore the importance of welding current as the dominant parameter, with welding time and pressure serving as complementary factors to fine-tune the process.

## 5. CONCLUSIONS

In this study, the Taguchi method was applied to optimize the RSW parameters for AISI 316L steel sheets. Taguchi technique was employed to determine the significance of each process parameter, while the predicted optimal parameters were experimentally validated by measuring tensile shear strength. Based on the findings, the following conclusions have been drawn:

Effect of welding time on nugget formation and temperature distribution: It was observed that an increase in welding time causes a rapid rise in the temperature at the faying surfaces of the sheets. This rise continues until the melting point of the material is reached, leading to the formation of a weld nugget. Once the nugget is formed, the rate of temperature increase diminishes abruptly. The absence of material expulsion during welding times of up to 8 cycles indicates that the welding time has a minimal impact on expulsion within this range. This finding underscores the importance of precise control over welding time to maintain weld integrity.

Impact of welding current on tensile shear strength: In resistance spot welding, welding current is a crucial factor since it directly affects the joint's tensile shear strength and the amount of heat generated required for nugget formation. Strong, flawless welds are guaranteed by current optimization, which balances heat input, reduces expulsion, and improves overall process efficiency.

Contribution of individual process parameters: Among the three process parameters evaluated, welding current exhibited the highest percentage contribution to the quality of the weld, while weld time played a moderate role. In contrast, welding pressure had the least influence on the overall process. These results emphasize the need for prioritizing welding current adjustments when optimizing the RSW process for AISI 316L steel sheets.

Optimal parameter: Both welding pressure and welding time were found to have a notable influence on the tensile shear strength of SS 316L sheet joints. For optimal joint strength, the recommended parameters are a welding current of 10 kA, an electrode force of 2 bars, and a welding time of 4 cycles per second.

**Author contributions:** conceptualization: S.D., D.D. and S.K.; data curation: A.C., S.A.; investigation: S.D.; methodology: A.C., S.A.; project administration: S.D.; resources: S.K.; software: S.A.; supervision: S.K. and S.D.; validation: S.D., D.D.; visualization: D.D.; initial draft writing: S.D.; review and editing: A.C., S.K.; funding acquisition. All authors have read and agreed to the published version of the manuscript.

**Funding source:** This paper has received no external funding.

**Conflicts of interest:** The authors declare that there are no conflicts of interest regarding the publication of this manuscript. We have no financial or personal relationships with individuals or organizations that could influence our work or could be perceived as potential conflicts of interest.

**Data availability statement:**

The data sets generated and/or analyzed during the current study are available from the corresponding author upon reasonable request. Restrictions may apply to the availability of certain data due to privacy or ethical concerns. However, the authors will make every effort to provide access to the data in accordance with applicable regulations and guidelines.

## REFERENCES


[1] De Castro, C. C., Shen, J., Plaine, A. H., Suhuddin, U. F., de Alcântara, N. G., dos Santos, J. F., Klusemann, B. (2022). *Tool wear mechanisms and effects on refill friction stir spot welding of AA2198-T8 sheets*. Journal of Materials Research and Technology, 20, 857-866.

[2] Chaudhari, A. Y., Deshmukh, D. D. (2020). *Metallurgical investigations on corrosion behavior of simple and heat treated duplex stainless steel 2205 exposed to corrosive media*. In IOP Conference Series: Materials Science and Engineering, 810(1), article number 012048.

[3] Xiao, R., Zhao, Y., Liu, H., Oliveira, J. P., Tan, C., Xia, H., Yang, J. (2022). *Dissimilar laser spot welding of aluminum alloy to steel in keyhole mode*. Journal of Laser Applications, 34(1), https://doi.org/10.2351/7.0000515

[4] Baek, S., Song, J., Lee, H. C., Park, S. Y., Song, K. H., Lee, S., Kim, D. (2022). *Robust bonding and microstructure behavior of aluminum/high-strength steel lap joints using resistance element welding process for lightweight vehicles: Experimental and numerical investigation*. Materials Science and Engineering: A, 833, 142378, https://doi.org/10.1016/j.msea.2021.142378Get rights and content

[5] Al-Ani, M. (2023). *Investigation of mechanical and microstructural characteristics of friction stir spot welded joints of aluminum sheets*. AIP Conference Proceedings, 2651(1), https://doi.org/10.1063/5.0105645

[6] Reza Kashyzadeh, K., Farrahi, G. H., Minaei, M., Masajedi, R., Gholamnia, M., Shademani, M. (2022). *Numerical study of shunting effect in three-steel sheets resistance spot welding*. International Journal of Engineering, 35(2), 406-416.

[7] Kalyankar, V., Bhoskar, A., Deshmukh, D., Patil, S. (2022). *On the performance of metallurgical behaviour of Stellite 6 cladding deposited on SS316L substrate with PTAW process*. Canadian Metallurgical Quarterly, 61(2), 130-144.

[8] Deshmukh, D. D., Kharche, Y. (2025). *Influence of processing conditions on the tensile strength and failure pattern of resistance spot welded SS 316L sheet joint*. International Journal on Interactive Design and Manufacturing (IJIDeM), 19(1), 559-571.

[9] Chen, L., Zhang, Y., Xue, X., Wang, B., Yang, J., Zhang, Z. Barber, G. C. (2022). *Investigation on shearing strength of resistance spot-welded joints of dissimilar steel plates with varying welding current and time*. Journal of Materials Research and Technology, 16, 1021-1028.

[10] Rajarajan, C., Sonar, T., Sivaraj, P., Raja, S., Mathiazhagan, N. (2022). *Investigating the effect of electrode pressure on nugget size, microstructure and tensile shear strength of resistance spot welded advanced high strength dual phase steel joints*. Metallography, Microstructure, and Analysis, 11(3), 472-483.

[11] Sachin K. Dahake, Nilesh Diwakar, Shyamkumar D. Kalpande (2023). *Optimization of Resistance Spot Welding Parameters for 316L Stainless Steel Using Response Surface Methodology and Box-Behnken Design: Investigation on Joint Characteristics and Performance*. Tuijin Jishu/Journal of Propulsion Technology, 44(5), doi: 10.52783/tjjpt.v44.i5.3003.

[12] Ghanbari, H. R., Shariati, M., Sanati, E., Nejad, R. M. (2022). *Effects of spot welded parameters on fatigue behavior of ferrite-martensite dual-phase steel and hybrid joints*. Engineering Failure Analysis, 134, 106079, https://doi.org/10.1016/j.engfailanal.2022.106079

[13] Betiku, O. T., Ramachandran, D. C., Ghatei-Kalashami, A., DiGiovanni, C., Sherepenko, O., Ghassemi-Armaki, H., Biro, E. (2023). *Improving the mechanical performance of press-hardened steel resistance spot welds via in-situ grain refinement*. Journal of Materials Processing Technology, 320, 118122, https://doi.org/10.1016/j.jmatprotec.2023.118122

[14] Dong, W., Lei, M., Pan, H., Ding, K., Gao, Y. (2022). *Role of the internal oxidation layer in the liquid metal embrittlement during the resistance spot welding of the Zn-coated advanced high strength steel*. Journal of Materials Research and Technology, 21, 3313-3326.

[15] Wippermann, J., Meschut, G., Koshukow, W., Liebsch, A., Gude, M., Minch, S., Kolbe, B. (2023). *Thermal influence of resistance spot welding on a nearby overmolded thermoplastic–metal joint*. Welding in the World, 67(3), 793-804.

[16] Zhao, D., Vdonin, N., Radionova, L., Glebov, L., Bykov, V. (2022). *Optimization of post-weld tempering parameters for HSLA 420 steel in resistance spot welding process*. The International Journal of Advanced Manufacturing Technology, 123(5-6), 1811-1823.

[17] Aswar S. J., Diwakar Nilesh, Kalpande S. D. (2023). *Investigations And Optimization of Laser Process Parameters Using Box Benhken Design Approach for Advanced Materials*. Journal of Aeronautical Materials, 43(1), 525-542.

[18] Kakade, S., Thakur, A., Patil, S., Deshmukh, D. (2023). *Experimental evaluation and correlation of plasma transferred arc welding parameters with hardfacing defects*. In Recent Advances in Material, Manufacturing, and Machine Learning, pp. 326-331, CRC Press, doi: 10.1201/9781003358596-34
[19] Guo, J., Bi, J., Wang, S., Li, Y., Manladan, S. M., Luo, Z. (2022). *Modelling the effect of electrode morphology on Mg/steel resistance spot welding*. The International Journal of Advanced Manufacturing Technology, 120(1-2), 137-148.
[20] Yaghoobi, F., Jamaati, R., Aval, H. J. (2022). *Resistance spot welding of high-strength DP steel and nano/ultrafine-grained IF steel sheets*. Materials Chemistry and Physics, 281, 125909, https://doi.org/10.1016/j.matchemphys.2022.125909
[21] Kakade, S. P., Thakur, A. G., Deshmukh, D. D., Patil, S. B. (2022). *Experimental investigations and optimisation of Ni-Cr-B-Si hardfacing characteristics deposited by PTAW process on SS 410 using response surface method*. Advances in Materials and Processing Technologies, 9(3), 826-842.
[22] Chaudhari A. Y., Diwakar Nilesh, Kalpande S. D. (2023). *Mechanical characteristics, morphology and corrosion behavior of duplex stainless steel 2205*. Eur. Chem. Bull. 12(8), 4900-4910.
[23] Naik, H. V., Deshmukh, D. D., Kalyankar, V. D. (2019). *Study of heat treatment effect on microstructure of PTA weld deposited surface of SS 316L steel*. In Advances in Additive Manufacturing and Joining: Proceedings of AIMTDR 2018, pp. 597-607, Singapore: Springer Singapore.
[24] Kalyankar, V. D., Deshmukh, D. D. (2017). *Failure investigations of failed valve plug SS410 steel due to cracking*. In IOP Conference Series: Materials Science and Engineering, 282(1), 012007.
[25] Deshmukh, D. D., Kalyankar, V. D. (2019). *Deposition Characteristics of Multitrack Overlay by Plasma Transferred Arc Welding on SS316Lwith Co-Cr Based Alloy–Influence of Process Parameters*. High Temperature Materials and Processes, 38(2019), 248-263.
[26] Deshmukh, D. D., Kalyankar, V. D. (2018). *Recent status of overlay by plasma transferred arc welding technique*. International Journal of Materials and Product Technology, 56(1-2), 23-83.
[27] Deshmukh, D. D., Kalyankar, V. D. (2019). *Evaluation of surface characteristics of PTAW hardfacing based on energy and powder supplied*. In Advances in Micro and Nano Manufacturing and Surface Engineering: Proceedings of AIMTDR 2018, pp. 547-558, Singapore: Springer Singapore.
[28] Ding, K., Dong, W., Lei, M., Wang, L., Pan, H., Gao, Y. (2022). *Oxidation-assisted crack propagation of the liquid metal embrittlement in the resistance spot welded steels*. Materials Characterization, 194, 112438, https://doi.org/10.1016/j.matchar.2022.112438
[29] Manladan, S. M., Jang, Y., Park, Y. D. (2023). *Effect of paint baking on the halo ring and mechanical behavior of 30MnB5 hot-stamped steel resistance spot welding joints*. Journal of Materials Research and Technology, 24, 4756-4761.
[30] Yang, Y., Li, Y., Bi, J., Liu, H., Ao, S., Luo, Z. (2022). *Microstructure and mechanical properties of 2195/5A06 dissimilar joints made by resistance spot welding*. Materials Characterization, 191, 112147, https://doi.org/10.1016/j.matchar.2022.112147
[31] Pestka, J., Weihe, S. (2022). *Influence of the Joining Force on the Nugget Diameter During Resistance Spot Welding of Aluminum Materials*. In Stuttgart Conference on Automotive Production, pp. 96-107, Cham: Springer International Publishing.
[32] Kumar, N., Ramakrishnan, S. M., Panchapakesan, K., Subramaniam, D., Masters, I., Dowson, M., Das, A. (2022). *In-depth evaluation of micro-resistance spot welding for connecting tab to 18,650 Li-ion cells for electric vehicle battery application*. The International Journal of Advanced Manufacturing Technology, 121(9-10), 6581-6597.
[33] Sharma, S. K., Patel, P., Chandra, M., Rajak, A. K., Sharma, C. (2022). *Resistance Spot Welding of Aluminum 6063 Alloy for Aerospace Application: Improvement of Microstructural and Mechanical Properties*. Journal of The Institution of Engineers (India), Series D, 103(1), 311-318.
[34] Bhoskar, A., Kalyankar, V., Deshmukh, D. (2023). *Metallurgical characterisation of multi-track Stellite 6 coating on SS316L substrate*. Canadian Metallurgical Quarterly, 62(4), 665-677.
[35] Hamidinejad, S., Kolahan, F., Kokabi, A. (2012). *The modelling and process analysis of resistance spot welding on galvanized steel sheets used in car body manufacturing*. Materials & Design, 34, 759-767. doi: 10.1016/j.matdes.2011.06.064.

Received: March 3rd, 2025 / Accepted: June 15th, 2025 / Paper available online: June 20th, 2025